Chemical Engineering Journal 476 (2023) 146785

Contents lists available at ScienceDirect

Chemical Engineering Journal

journal homepage: www.elsevier.com/locate/cej

The inhibitory mechanism of humic acids on photocatalytic generation of reactive oxygen species by TiO_2 depends on the crystalline phase

Youn-Jun Lee [a], Yoo Jae Jeong [a,b], In Sun Cho [a,b], Chang-Gu Lee [a,c,*], Seong-Jik Park [d], Pedro J.J. Alvarez [e]

[a] Department of Energy Systems Research, Ajou University, Suwon 16499, South Korea
[b] Department of Materials Science & Engineering, Ajou University, Suwon 16499, South Korea
[c] Department of Environmental & Safety Engineering, Ajou University, Suwon 16499, South Korea
[d] Department of Bioresources & Rural System Engineering, Hankyong National University, Anseong, South Korea
[e] Department of Civil and Environmental Engineering, Rice University, Houston, TX 77005, USA

ARTICLE INFO

Keywords:
Natural organic matter
TiO_2
Humic acids
Crystalline phase
Reactive oxygen species
Photocatalytic oxidation

ABSTRACT

To enable the practical use of TiO_2 for photocatalytic water treatment, it is important to understand how dissolved natural organic matter affects its photocatalytic activity and the mechanisms involved in generating reactive oxygen species (ROS). In this study, we systematically investigated the inhibitory effects of humic acids (HA) on 4-chlorophenol (4-CP) degradation using two common TiO_2 crystalline phases (anatase and rutile) individually. HA strongly hindered the photocatalytic activity of anatase, with an R_a (the ratio of the first-order rate constant for 4-CP degradation in the absence vs. presence of 30 mg/L HA) of 2.30 (±0.13). This ratio was significantly higher than that of rutile ($R_r = 1.21 \pm 0.08$), which was less susceptible to this inhibitory effect and even exhibited improved photocatalytic activity at HA concentrations below 20 mg/L. Similar trends were observed for various HA sources, corroborating the crystalline-phase-dependent effect of HA. Adsorption experiments, Fourier transform infrared spectroscopy, and photoelectrochemical analyses suggested that the adsorption mechanisms and hole-scavenging effect of HA on the two TiO_2 polymorphs did not differ. Importantly, scavenger, probe, and electron spin resonance experiments revealed that the difference in inhibitory effects of HA originate from the distinct ROS generation mechanisms for the two polymorphs. The oxygen reduction pathway for $^{\bullet}OH$ generation over anatase was hindered by surface-adsorbed HA, while the water oxidation pathway for $^{\bullet}OH$ generation over rutile was less affected. Furthermore, surface-adsorbed HA boosted $O_2^{\bullet-}$ generation on rutile, increasing 4-CP degradation efficiency. This mechanistic insight into NOM-TiO_2 interactions informs materials selection and strategies for higher TiO_2 photocatalytic performance in different water matrices.

1. Introduction

Photocatalytic oxidation has been extensively studied due to its significant potential as an environmentally friendly, cost-effective, and highly efficient approach to water purification without adding treatment chemicals [1–3]. Accordingly, various photocatalysts have been designed and tested for the degradation of organic pollutants [4–6]. Titanium dioxide (TiO_2), which is the most widely studied photocatalyst, currently appears to be the most feasible for practical use due to its natural abundance and relatively low cost. However, the presence of dissolved natural organic matter (NOM) in natural water sources and wastewater hinders the efficiency of TiO_2 to enable the photocatalytic degradation of target organic pollutants [7]. In particular, humic acids (HA), a common form of NOM found in water, are known to significantly hinder the photocatalytic activity of TiO_2 in various ways [8].

TiO_2 tends to adsorb HA via electrostatic attraction, hydrophobic interactions, and ligand exchange with abundant functional groups found in HA (e.g. hydroxyl, phenolic, and carboxy groups) [9], and surface-bound HA can hinder the reactive oxygen species (ROS) generation and the target pollutant degradation [10]. Dissolved HA can also decrease overall efficiency via light attenuation [11] and ROS scavenging [12]. However, HA has the potential to increase the

* Corresponding author at: Department of Energy Systems Research, Ajou University, Suwon 16499, South Korea.
E-mail address: changgu@ajou.ac.kr (C.-G. Lee).

https://doi.org/10.1016/j.cej.2023.146785
Received 23 July 2023; Received in revised form 20 September 2023; Accepted 17 October 2023
Available online 19 October 2023

photocatalytic performance of TiO_2. In particular, the direct energy transfer of excited triplet-state HA [13], singlet oxygen generation [8], and ligand-to-metal charge transfer (LMCT) [14] can have a positive effect on the organic pollutant degradation. Due to its significance, numerous studies have investigated the effect of HA in TiO_2-based photocatalysis systems designed to degrade various refractory organic pollutants [15–17]. Nevertheless, most previous studies have focused on examining the degradation efficiency of target pollutants after the introduction of HA, while the specific mechanisms by which HA affects the behavior of TiO_2 and the ROS generation pathways have rarely been systematically studied.

In TiO_2-based photocatalysis oxidation, ROS play a crucial role as primary intermediates, directly influencing both the mechanisms and efficiency of organic pollutant degradation. Photoinduced electrons and holes on the surface of heterogeneous photocatalysts engage in redox reactions with adsorbed molecules such as H_2O and O_2, resulting in the primary ROS generation, including hydroxyl radicals ($^{\bullet}OH$), superoxide radicals ($O_2^{\bullet-}$), and hydrogen peroxide (H_2O_2) [18]. The generation pathway for ROS varies based on the characteristics of TiO_2, such as its morphology, optical and electronic structure, and surface properties [19,20]. Because strongly adsorbed HA can alter some of these attributes, it can also affect the ROS generation pathways. For example, a higher concentration of H_2O_2 can be generated in situ via the direct reduction of O_2 over HA-adsorbed P25 TiO_2 compared with pristine TiO_2 under visible light irradiation [14]. Given the complex effects HA can have on TiO_2-based photocatalysis, we postulate that changes in ROS generation and the degradation efficiency of TiO_2 for target pollutants following HA adsorption are dependent on the specific characteristics of TiO_2.

The crystalline phase of TiO_2 governs its properties [21], which in turn dictate its photocatalytic activity. The TiO_2 polymorphs anatase and rutile have been widely utilized as photocatalysts, with numerous studies examining their synthesis methods [22], photocatalytic behavior [23], reactivity with specific molecules [24], and interaction with co-catalysts [25]. However, little is known about how the crystalline phase of TiO_2 affects its susceptibility to inhibition by surface-adsorbed HA, and the resulting effects on different photocatalytic ROS generation pathways.

In this study, we compare the inhibitory effects of HA on the degradation of the common water pollutant 4-chlorophenol (4-CP), using anatase and rutile TiO_2 photocatalysts individually. 4-CP is refractory organic pollutant, which is commonly discharged from many industries and agriculture [26]. Due to the high reactivity toward ROS [27], 4-CP was selected as target pollutant. Increasing the HA concentration (1–30 mg L^{-1}) decreased the photocatalytic activity of anatase under UV illumination, while rutile was less susceptible to this negative effect and even exhibited improved photocatalytic activity when HA was present at concentrations below 20 mg L^{-1}. To determine the mechanisms responsible for these different responses, the effect of HA on ROS generation by the two polymorphs was investigated. Results revealed that differences in the $^{\bullet}OH$ generation pathways for two polymorphs were responsible for the crystalline-phase-dependent susceptibility to imbibition by HA. This study thus offers mechanistic insight into the interactions between NOM and TiO_2, and informs materials selection for more efficient application of TiO_2 in photocatalytic treatment of different water matrices.

2. Materials and methods

2.1. Materials

TiO_2 (P25, 99.5 %), 4-CP (C_6H_5ClO, 99 %), HA, benzoic acid (BA, $C_7H_6O_2$, 99.5 %), and nitro blue tetrazolium (NBT, $C_{40}H_{30}N_{10}O_6\bullet 2Cl$, 90 %) were purchased from Sigma-Aldrich. Suwanee River humic acid (SRHA, Standard III) was purchased from International Humic Substances Society. Aladdin humic acid (AHA) was purchased from Aladdin Industrial Corporation. Tert-butanol (TBA, $C_4H_{10}O$, 99 %), hydrogen peroxide (H_2O_2, 34.5 %), hydrofluoric acid (HF, 49 %), and ammonium hydroxide (NH_4OH, 25 %) were purchased from Samchun Chemicals. In addition, p-hydroxybenzoic acid (p-HBA, $C_7H_6O_3$, 99 %) was purchased from Junsei Chemical, while 5–5-dimethyl-1-pyrroline N-oxide (DMPO, $C_6H_{11}NO$, 97 %) was purchased from TCI Chemicals. Throughout all conducted experiments, ultrapure water with a resistivity of 18.2 MΩ•cm was produced using a Millipore direct 3 UV water purification system.

2.2. Preparation of TiO_2 polymorphs

Anatase and rutile TiO_2 nanoparticles were prepared from the same P25 photocatalyst to ensure that, except for the crystalline phase, their physiochemical characteristics were similar (Fig. S1-3). Selective chemical etching methods using H_2O_2-NH_3 or HF solutions were employed to obtain anatase and rutile nanoparticles, respectively [28,29]. For the preparation of anatase, 0.5 g of P25 was added to the 55 mL of NH_3-H_2O_2 solution (5 mL of 2.5 % NH_4OH + 50 mL of 30 % H_2O_2). After stirring for 12 h, the separated anatase nanoparticles were washed using DI several times. For the preparation of rutile, 2.0 g of P25 was added to the 100 mL of 10 % HF solution. Then, the suspension was stirred for 24 h and the separated rutile nanoparticles were washed several times using DI until neutral pH. The transmission electron microscope (TEM) was used to examine the morphology and crystal phase of anatase, rutile, and P25 (Fig.S2). The prepared anatase and rutile nanoparticles displayed lattice spacings of 0.35 nm (corresponding to the (1 0 1) plane) (Fig. S2c) [30] and 0.32 nm (corresponding to the (1 1 0) plane) (Fig. S2f) [31], respectively, which were matched that of the anatase and rutile phases in P25 (Fig. S2i). The crystalline phase of the polymorphs was confirmed using X-ray diffractometer (XRD) and Raman spectra (Fig. S1a, b). The crystallite size of the anatase and rutile derived from the XRD analysis was 12.1 and 15.8 nm, respectively. Other analyses of the polymorphs, including the zeta potential, Brunauer-Emmett-Teller (BET) surface area, and field-emission scanning electron microscopy (FE-SEM), were also conducted (Fig. S1c–f).

2.3. Characterization

The morphologies of TiO_2 polymorphs were examined on TEM (JEM-3010, JEOL). The crystalline phase of the TiO_2 polymorphs was analyzed using X-ray diffraction (XRD, D/max-2500 V, Rigaku) and a high-resolution Raman spectrometer (excitation wavelength = 325 nm, LabRam HR Evolution, Horiba). The surface functional groups of HA and TiO_2 were analyzed by Fourier-transform infrared spectroscopy (FT-IR, Nicolet is50, Thermo). The surface electrical charge of HA and TiO_2 was analyzed using a zeta potential analyzer (ELSZ-2000ZS, Otsuka Electronics). The BET surface area of TiO_2 samples was analyzed using an adsorption analyzer (ASAP 2020, Micrometrics), while the morphologies of the prepared TiO_2 samples were observed using FE-SEM (JSM-7900F, JEOL). Excitation-emission matrix (EEM) of HA was analyzed using photoluminescence spectrometer (FS5, Edinburgh Instruments). The generated ROS were determined using electron spin resonance (ESR, EMXplus-9.5/12/P/L system, Bruker) with DMPO as a trapping agent. Details of the experimental ESR procedure are provided in Text S1. The photocurrent of the TiO_2 samples was analyzed using a photoelectrochemical system. The photocurrent was recorded using potentiometer (SP-200, Biologics). The reference and working electrodes were Ag/AgCl, and Pt wire, respectively. The experimental procedure is described in Text S2.

2.4. Photocatalytic experiments

The quartz reactor (total volume of 70 mL) was used to carry out the photocatalytic reaction, which was placed in the middle of a black acrylic box outfitted with six UV-A lamps (λ_{max} = 365 nm, TL 4 W BLB,

Philips). The light intensity inside the quartz reactor using ferrioxalate actinometry was determined to be 3.93×10^{-9} Einstein cm^{-2} s^{-1} [32]. The emission spectra of UV-A lamp inside and outside of the quartz reactor is provided in Fig. S4. To investigate the effect of HA on the pollutant removal efficiency of the two polymorphs, an HA stock solution was spiked into a TiO_2 suspension (0.2 g L^{-1}) containing 4-CP (5 mg L^{-1}). To reach the adsorption–desorption equilibrium, 50 mL of the solution was magnetically stirred in the dark for 30 min. The initial pH of the solution was adjusted to 6.5 (±0.2) for all experiments. During UV-A irradiation, 1 mL aliquots were taken using a PTFE syringe filter, and the 4-CP concentration was measured immediately using high-performance liquid chromatography (YL 9120) equipped with a UV/vis detector. The separation of the mobile phase, composed of acetonitrile and 0.1 % formic acid in a ratio of 40:60, was conducted using a C18 column (4.6 mm × 150 mm × 5 μm) at a flow rate of 1 mL/min. The stability of anatase and rutile was tested in same photocatalytic experiment conditions. After reuse of photocatalyst, the solution was centrifuged and 4-CP concentration in the supernatant was measured. Then, the recovered photocatalysts were used for subsequent photocatalytic experiment. The same concentration of HA (20 mg L^{-1}) was added for each cycle. The stability test was conducted in 3 cycles. The 4-CP degradation product was analyzed using liquid chromatography-mass spectrometer. The electrospray ionization source was operated in negative mode. The analysis was conducted under following settings: spray voltage: 3 kV, vaporizer temperature: 400 °C, capillary temperature: 250 °C. In addition, the degradation of nitro blue tetrazolium (NBT) was recorded by substituting 4-CP with NBT. The initial concentration of NBT was 50 μM and the concentration was determined using a UV spectrophotometer (UV-1800, SHIMADZU) at 260 nm. The first-order rate constant for 4-CP degradation (k) was determined as the slope of a linear regression of 4-CP concentration versus time data. The inhibitory effect of HA on the photocatalytic activity of polymorphs was represented by the R value, which is the ratio between the reaction rate constant for 4-CP degradation with and without HA ($k_{w/o\ HA}/k_{w/HA}$). The error for the R value was determined using the error propagation method described in Text S3.

HA adsorption was recorded in the same quartz reactor without 4-CP and UV-A irradiation. The amount of HA adsorbed onto the surface of the two polymorphs was determined by measuring the concentration of HA using a UV spectrophotometer at 254 nm. The H_2O_2 concentration generated during photocatalysis was measured using iodine titration [33]. All of the photocatalytic experiments were conducted in triplicate (n = 3) and the standard deviation from the mean was represented as error bars. The statistical significance of differences between experimental results was assessed using a two-tailed *t*-test at the 95 % confidence level.

3. Results and discussion

3.1. HA has a more pronounced inhibitory effect on anatase than on rutile

4-CP degradation patterns were characterized in the presence and absence of HA, and R values for anatase (R_a) and rutile (R_r) were determined for various HA concentrations, from 1 to 30 mg L^{-1} (Fig. 1a, b). HA showed notable inhibitory effect on 4-CP degradation using anatase, and R_a increased from 1.10 ± 0.13 to 2.30 ± 0.13 as HA concentrations increased from 1 to 30 mg L^{-1}. In contrast, rutile was less susceptible to this inhibitory effect and even exhibited improved photocatalytic activity at the lower tested HA concentrations. Specifically, the highest 4-CP degradation rate was observed with 5 mg L^{-1} HA (R_r = 0.88 ± 0.05), and R_r was lower than 1 for rutile at an HA concentration range of 1–20 mg L^{-1}. Apparently, the positive effect of HA on the photocatalytic activity of rutile outweighed its negative effect. Because 4-CP was not directly degraded by UV irradiation in the presence of HA alone (Fig. S5), the positive effect of HA on 4-CP degradation by rutile can be attributed to the effect of HA adsorbed on the rutile surface,

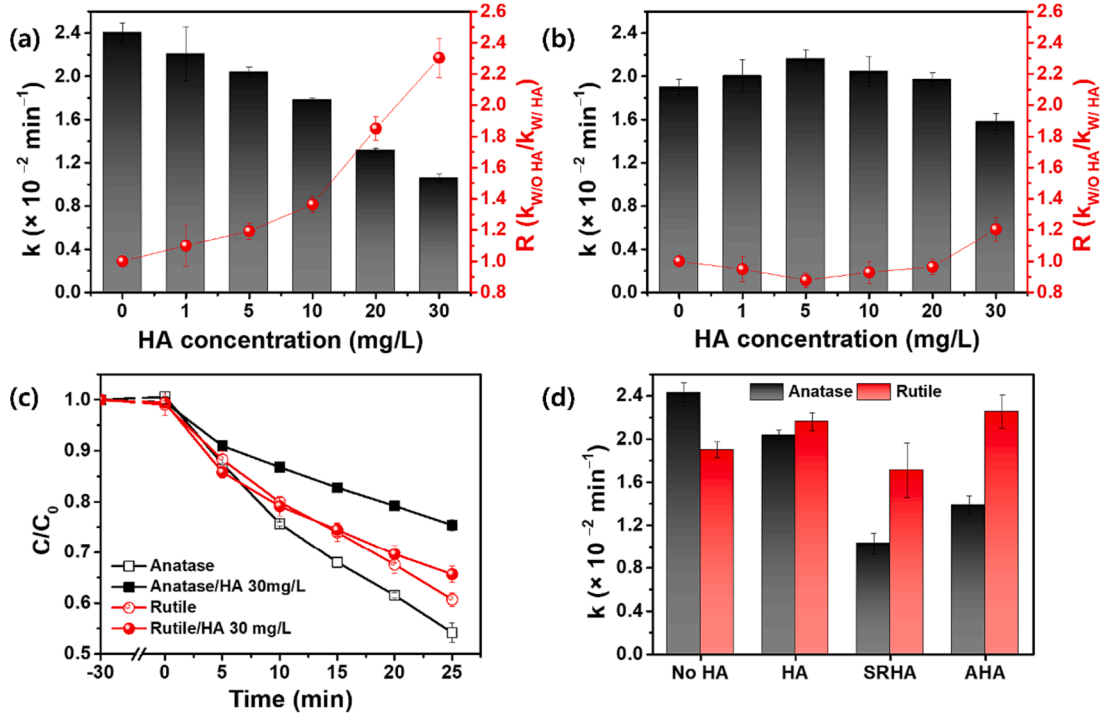

Fig. 1. HA significantly decreases the photocatalytic degradation efficiency of 4-CP with anatase, but not with rutile. The first-order degradation rate constant for 4-CP and R values for (a) anatase and (b) rutile are presented. (c) Time profiles of 4-CP degradation kinetics show that rutile has higher photocatalytic degradation efficiency in the presence of HA (30 mg/L). (d) A similar trend in 4-CP degradation efficiency in the presence of other HA sources confirms the crystalline-phase-dependent inhibitory effect of HA (5 mg/L) on the photocatalytic activity of TiO_2 (experimental conditions: $[4\text{-CP}]_0$ = 5 mg/L, pH = 6.5 ± 0.2, photocatalyst dose: 0.2 g/L).

which can alter ROS generation (as discussed in Section 3.3). Furthermore, the inhibitory effect of 30 mg L^{-1} HA was significantly lower than that for anatase (R_r was 1.21 ± 0.08, versus 2.30 ± 0.13 for R_a) ($p < 0.05$).

Fig. 1c and S6 present the time profiles and first-order kinetic curves for 4-CP degradation over anatase and rutile in the presence of HA (30 mg/L). The removal of 4-CP via adsorption onto the photocatalyst both with and without HA was negligible, implying that the degradation of 4-CP mainly occurred in the bulk solution [34]. Without HA, anatase exhibited a higher 4-CP degradation rate (2.40 ± 0.09 × 10^{-2} min^{-1}) than rutile (1.90 ± 0.07 × 10^{-2} min^{-1}) due to its inherently superior photocatalytic activity, which is consistent with previous studies [35–37]. However, when 30 mg/L of HA was present, the 4-CP degradation rate for anatase drastically decreased, while that of rutile only slightly decreased. As a result, rutile exhibited a higher 4-CP degradation rate (1.58 ± 0.08 × 10^{-2} min^{-1}) than anatase (1.06 ± 0.04 × 10^{-2} min^{-1}) with 30 mg/L HA. This indicates that HA differs in its inhibitory effects depending on the TiO_2 crystalline phase. In comparison with the separated anatase and rutile, P25 showed much higher photocatalytic activities in the absence of HA (Fig. S7), which can be attributed to the charge transfer between interconnected anatase and rutile [38]. However, P25 (80 % anatase) showed the lower 4-CP degradation rate (1.55 ± 0.26 × 10^{-2} min^{-1}) than rutile in the presence of 30 mg/L HA with the highest R value (8.18 ± 1.18), which probably attributed to its high anatase content.

To further corroborate the crystalline-phase-dependent inhibitory effects of HA, the 4-CP degradation rate in the presence of other HA sources (SRHA and AHA) was evaluated (Fig. 1d). Consistent with the HA results, a stronger inhibitory effect was observed for anatase with SRHA or AHA (5 mg L^{-1}), hence rutile exhibited a significantly higher 4-CP degradation rate. In particular, AHA increased the photocatalytic activity of rutile compared to HA-free control tests. Overall, the similar trends observed for the HA isolates from different sources despite the differences in their properties (e.g., functional groups and EEM spectra) (Fig. S8). Additionally, higher resistance to inhibitory effect of fulvic acid was observed for rutile (Fig. S9), which corroborate that the inhibitory effect of HA strongly depends on the crystalline phase of TiO_2.

3.2. Adsorbed HA enhances photocatalytic reduction pathway for both polymorphs

To confirm that the adsorbed HA played a role in the inhibition of 4-CP degradation, other potential factors were ruled out. XRD diffraction peaks for the anatase and rutile phase did not disappear after HA adsorption, and no new peaks were detected (Fig. S1a), indicating that the HA did not change the crystal structure of TiO_2. Given the low light absorption of HA in the UV-A range (Fig. S10) [39], the light screening of HA was unlikely to be a major factor in its inhibitory effect. Therefore, the HA adsorption on the surface of photocatalyst was determined to be the most plausible reason for the different inhibitory effects of HA on the two polymorphs.

The adsorption kinetics of HA (30 mg/L) for the two polymorphs were investigated using an identical setup to that for the photocatalysis experiment but without light irradiation (Fig. 2a). The rapid adsorption of HA onto both polymorphs, reaching equilibrium within 30 min, was in accordance with previous findings [39,40]. The estimated amount of HA adsorbed onto anatase (29.0 ± 0.2 mg g^{-1}) after 30 min was about 1.4 times higher than that onto rutile (21.1 ± 1.9 mg g^{-1}). The equilibrium adsorption isotherms for the two polymorphs revealed a similar trend (Fig. 2b). The adsorption isotherm curves rapidly reached a plateau and closely followed the Langmuir isotherm model [41]. These results indicate similar HA adsorption mechanisms for the two

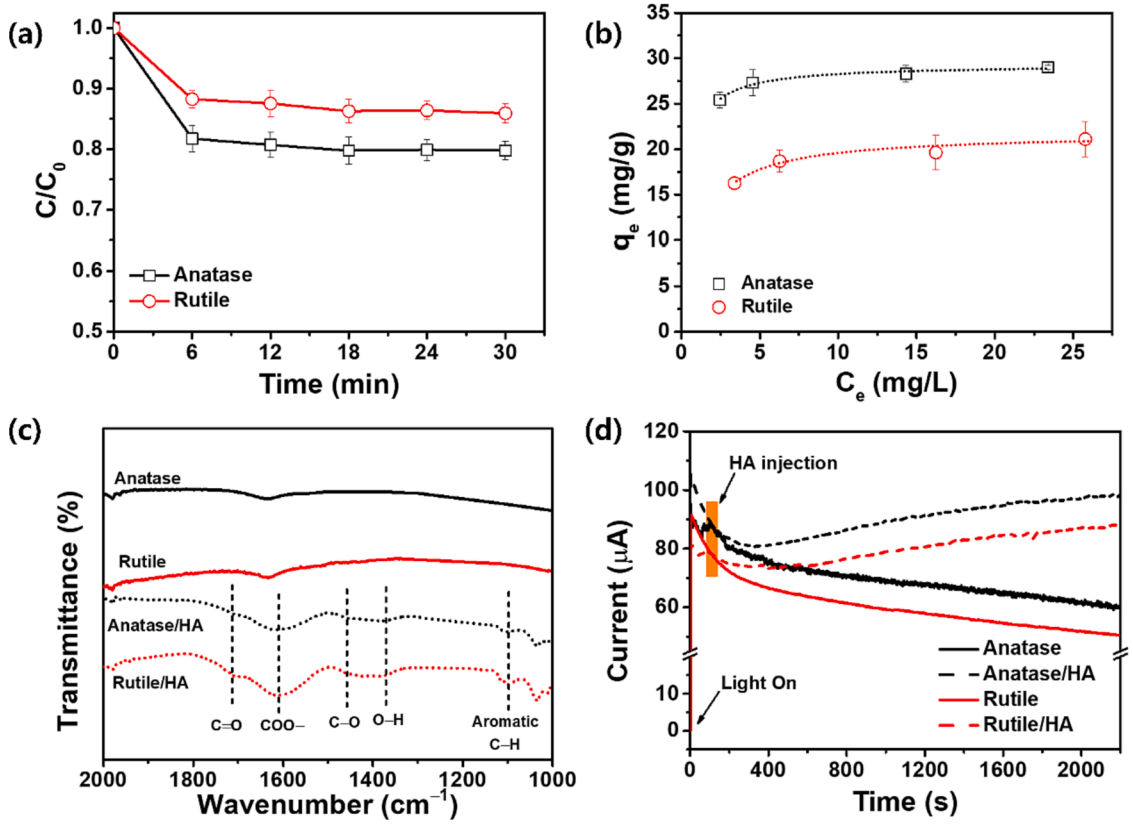

Fig. 2. Anatase and rutile show the same adsorption mechanisms (ligand exchange for HA: (a) HA adsorption kinetics ($[HA]_0$ = 30 mg/L) and (b) isotherms and (c) the FT-IR spectra for the pristine and HA-adsorbed polymorphs. The hole-scavenging effect of the donated electrons from the surface-adsorbed HA is reflected in (d) photocurrent analysis (experimental conditions: $[4\text{-CP}]_0$ = 5 mg/L, pH = 6.5 ± 0.2, photocatalyst dose: 0.2 L^{-1}).

polymorphs; hence, the higher amount of HA adsorbed on the surface of anatase can be mainly attributed to its higher specific surface area (anatase = 52.2 m^2/g and rutile = 31.6 m^2/g; Fig. S1c).

At near-neutral pH, the electrostatic attraction between the two polymorphs and HA is weak (Fig. S1d). Thus, another primary interaction mechanism was assumed to be in operation, which was investigated via FT-IR analysis (Fig. 2c). Compared to the pristine samples, new spectrum peaks at around 1704 (stretching of C═O), 1621 (asymmetric stretching of COO), 1454 (coupled C—O stretching), 1385 (in-plane bending vibration of OH), 1250 (C—OH of phenolic OH), and 1100 cm^{-1} (aromatic C—H deformation) were identified for both anatase and rutile after HA adsorption [39,42]. This indicates that the HA was adsorbed onto the two polymorphs through ligand exchange [9]. We also investigated the effect of surface-adsorbed HA on the behavior of photoinduced charge carriers by monitoring the photocurrent (Fig. 2d). The morphological appearance of anatase and rutile coated on FTO glass (thickness of ≈310 nm) did not exhibit any discernible difference from powder samples (Fig. S11). Compared to the pristine samples, the steady-state photocurrent of the two polymorphs increased after HA stock solution injection, indicating that more electrons were transferred into the external circuit due to the suppressed charge recombination of TiO_2. This indicate that HA scavenged the VB holes of TiO_2, inhibiting

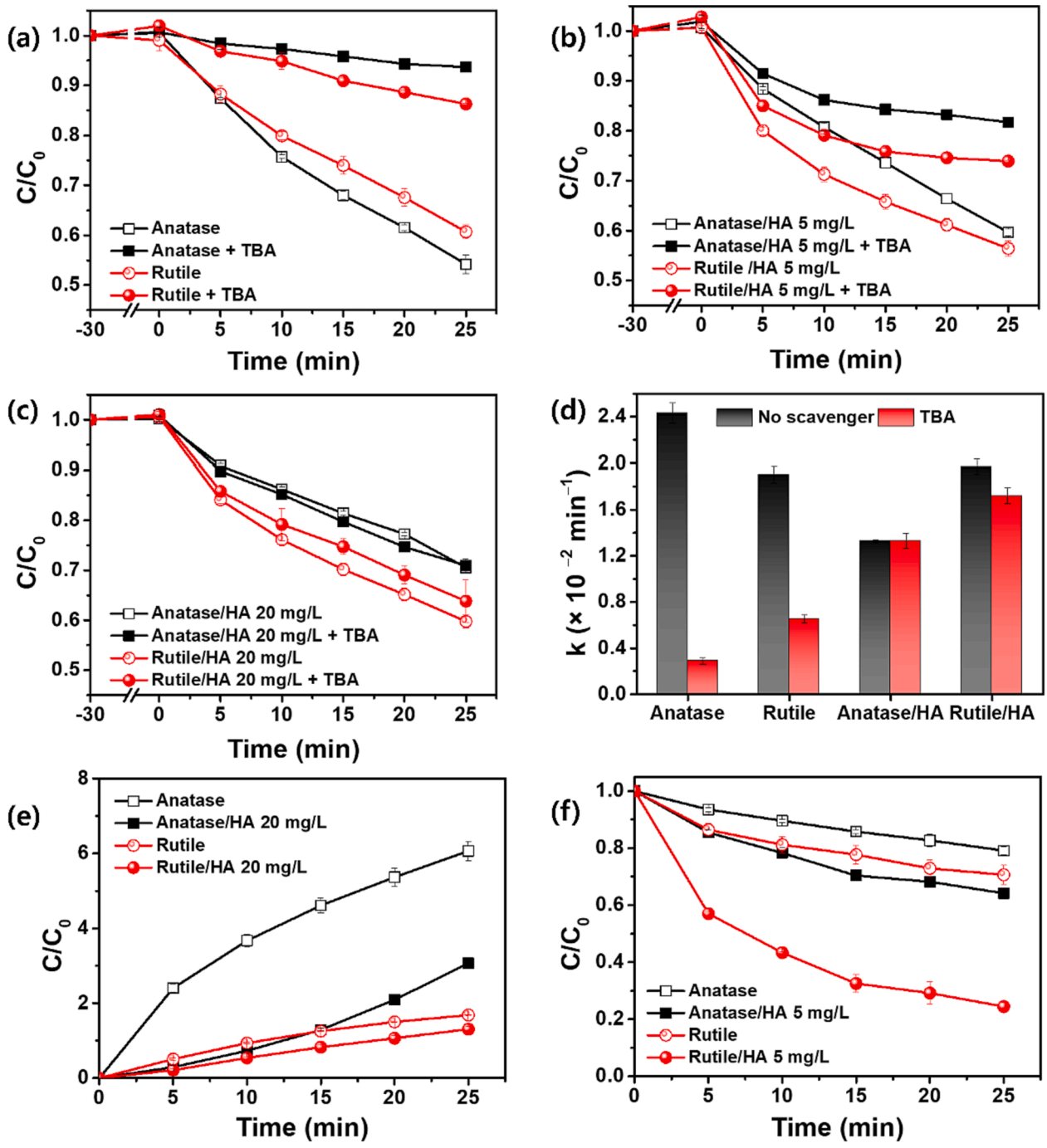

Fig. 3. HA notably reduces the contribution of ˙OH to 4-CP degradation, as illustrated by the effect of ˙OH-scavenging by TBA on 4-CP degradation in the presence of (a) 0, (b) 5, and (c) 20 mg/L HA. Panel (d) compares the degradation rate constant after the addition of TBA in the absence or presence of HA (20 mg/L). Probe tests using (e) BA and (f) NBT illustrate the lower ˙OH generation and higher $O_2^{\cdot-}$ generation in the presence of HA, respectively (experimental conditions: $[4\text{-CP}]_0 = 5$ mg/L, [TBA] = 100 mM $[BA]_0 = 0.4$ mM, $[NBT]_0 = 50$ μM, pH = 6.5 ± 0.2, photocatalyst dose = 0.2 L^{-1}).

the electron-hole recombination [39]. The adsorbed HA had electron-donating components (e.g., phenolic groups) [43] that likely enabled photocatalytic reduction over the two polymorphs. Overall, due to the similar adsorption and photocurrent trends for the two polymorphs, the reasons for the different inhibitory effects on their photocatalytic performance due to surface-adsorbed HA required further investigation.

3.3. HA suppresses $^{\bullet}OH$ generation while promoting $O_2^{\bullet-}$ generation

The transfer of electrons from adsorbed HA to TiO_2 during the photocatalytic reactions can alter the pathways for oxidative and reductive ROS production. $^{\bullet}OH$ is an important ROS in TiO_2-based photocatalytic treatment due to its high oxidation potential [44]. Thus, we used TBA as a scavenger of $^{\bullet}OH$ ($k = 6.0 \times 10^8\ M^{-1}\ s^{-1}$) [12] to investigate the contribution of $^{\bullet}OH$ to 4-CP degradation under varying concentrations of HA. In the absence of HA, the 4-CP degradation rates of the two polymorphs were notably lower when TBA was added, indicating that $^{\bullet}OH$ is the primary ROS for the photocatalytic degradation of 4-CP (Fig. 3a). The degradation product of $m/z = 143$ (4-chlrorocatechol or 4-chlororesorcinol), which is attributed to the reaction between 4-CP and $^{\bullet}OH$ [45] was detected after photocatalytic reaction (Fig. S12). The inhibitory effect of TBA on both polymorphs was less pronounced when 5 mg L^{-1} HA was present (Fig. 3b). Increasing the initial concentration of HA to 20 mg L^{-1} resulted in a negligible effect of TBA with anatase (likely due to a lower $^{\bullet}OH$ concentration), and only slight inhibition with rutile (Fig. 3c, d), indicating that the contribution of $^{\bullet}OH$ to 4-CP degradation decreased with increasing HA levels. Note that the gap in 4-CP degradation efficiency with and without TBA widened as the photocatalytic reaction progressed when initial HA concentration was 5 mg L^{-1}. As shown in Section 3.2, the amount of adsorbed HA was comparable for an HA concentration range of 5–30 mg L^{-1}, but the initial HA concentration had a distinct effect in the TBA scavenger tests. During photocatalysis, the valence band holes of TiO_2 oxidize adsorbed HA, which means no additional electron donors are available as the reaction proceeds when the initial concentration of HA is insufficient (5 mg L^{-1}). Consequently, when all of the HA was consumed, the ROS generation mechanism was similar to the case when HA was not absorbed. However, when sufficient HA was added (20 mg L^{-1}), HA continued to scavenge the TiO_2 holes (Fig. S13a), allowing the same reaction mechanism to be maintained until the end of the reaction. When comparing the EEM spectra before and after the reaction, the reduction in the maximum peak at 250/440 nm (Fig. S13b, c), which is associated with humic-like substances [46], serves as confirmation that the photocatalytic reaction leads to the oxidation of HA. The fouling of HA oxidation product on the TiO_2 surface reduces the photocatalytic performance [47], hence we further performed the cyclic tests (Fig. S14). After first cycle, the 4-CP degradation efficiency was notably decreased, indicating the oxidation of HA. As a result, the increase in R_a with increasing HA concentration despite a comparable amount of HA adsorption was due to the continuous hole scavenging at high initial HA concentrations.

ESR analysis and probe testing using BA were subsequently conducted to investigate the effect of surface HA on $^{\bullet}OH$ generation. In the ESR analysis, the intensity of the typical DMPO-OH signal for anatase was significantly weaker after HA adsorption, while that of rutile only slightly decreased (Fig. S15a). Consistent with this, the concentration of pHBA, which is generated in the reaction between BA and $^{\bullet}OH$, was notably lower with anatase after HA adsorption (Fig. 3e). Given that HA had the same effect on the behavior of the charge carriers in the two polymorphs, the difference between them in terms of $^{\bullet}OH$ generation after HA adsorption may originate from different $^{\bullet}OH$ generation pathway, which is discussed in Section 3.4. Although $^{\bullet}OH$ generation over rutile slightly decreased, it exhibited enhanced photocatalytic activity when the HA concentration was lower than 20 mg L^{-1} (Fig. 1b), suggesting that other types of ROS participate in the reaction.

Fig. 3f shows the relative concentration of the $O_2^{\bullet-}$ probe NBT during photocatalysis. The decay of NBT in the presence of the two polymorphs increased after the adsorption of HA (5 mg L^{-1}), indicating higher $O_2^{\bullet-}$ generation [48]. Adsorbed HA consumes the holes of TiO_2 and inhibits electron–hole pair recombination [49], hence more electrons migrate from the bulk to the photocatalyst surface to participate in the O_2 reduction reaction, producing more $O_2^{\bullet-}$ ($O_2 + e_{cb} \rightarrow O_2^{\bullet-}$). The higher generation of $O_2^{\bullet-}$ after HA adsorption was confirmed using ESR analysis (Fig. S15b). It should be noted that the NBT decay over rutile was notably higher than over anatase after HA adsorption even though the 4-CP degradation rates with anatase ($2.04 \pm 0.04 \times 10^{-2}\ min^{-1}$) and rutile ($2.16 \pm 0.08 \times 10^{-2}\ min^{-1}$) were comparable under the same experimental conditions. The surface structure of rutile can create more favorable conditions for the stabilization of $O_2^{\bullet-}$ due to its much higher oxygen vacancy density [50–52], thus enhancing the participation of $O_2^{\bullet-}$ in reaction. As a result, the notable increase in $O_2^{\bullet-}$ production offset the slightly lower $^{\bullet}OH$ production, leading to an increase in overall 4-CP degradation using rutile.

3.4. HA inhibits H_2O_2 adsorption on anatase

As shown in Section 3.3, the lower $^{\bullet}OH$ generation after HA adsorption was directly related to a higher R_a. To clarify the reasons for the higher inhibitory effect of HA on anatase compared to rutile, the $^{\bullet}OH$ generation pathway was investigated. $^{\bullet}OH$ generation when using TiO_2 in an aqueous environment generally includes an oxidative path (oxidation of water by valence band holes) and a reductive path (multi-step reduction of O_2 by conduction band electrons) [51]. Anatase and rutile differ in their mechanistic behavior during ROS generation, including variation in the lifetime of conduction band electrons [18] and the affinity toward reactant molecules (e.g. H_2O_2) [53], because they have different electronic and surface characteristics.

To gain a clearer understanding of the $^{\bullet}OH$ generation pathways for the two polymorphs, chromate (Cr(VI)) was introduced as an alternative electron acceptor during the photocatalytic degradation of 4-CP (Fig. 4a). The addition of Cr(VI) resulted in the significant inhibition of 4-CP degradation with anatase ($p < 0.05$) [44], whereas only a slight increase was observed for rutile. This indicates that the two polymorphs differed in their dominant pathway for $^{\bullet}OH$ generation, with anatase primarily using O_2 reduction, while rutile predominantly oxidized H_2O, which is consistent with previous studies [44,54]. With anatase, Cr(VI) reacted with the electrons, hindering the oxygen reduction reaction. To further confirm this, scavenger test using p-BQ ($O_2^{\bullet-}$ scavenger) [55] and KI (hole scavenger) [56] was conducted (Fig. S16) in the absence and presence of HA (20 mg L^{-1}). When p-BQ was added, 4-CP degradation was notably inhibited but the addition of KI showed only slight decrease in 4-CP degradation compared to control, indicating that oxygen reduction reaction was the major pathway for ROS generation over anatase. In contrast, the reaction between the electrons and Cr(VI) reduced electron–hole pair recombination in rutile, increasing the number of holes available for $^{\bullet}OH$ generation via water oxidation. The adsorption of HA enhanced the participation of the conduction band electrons by reducing electron–hole recombination. Thus, the production of $O_2^{\bullet-}$ over the two polymorphs increased, as confirmed by the NBT decay and ESR results. As a result, the greater production of $O_2^{\bullet-}$ over rutile after HA adsorption offset the lower generation of $^{\bullet}OH$. However, for anatase, the higher production of $O_2^{\bullet-}$ after HA adsorption did not lead to greater $^{\bullet}OH$ generation even though the reductive pathway was dominant for $^{\bullet}OH$ generation ($O_2 \rightarrow O_2^{\bullet-} \rightarrow H_2O_2 \rightarrow {}^{\bullet}OH$).

To identify the rate-determining step in the $^{\bullet}OH$ generation process, we compared the H_2O_2 concentration generated in situ over anatase with and without HA (Fig. 4b, S17). Compared to the pristine sample, the accumulation of H_2O_2 notably increased in the presence of HA, suggesting that the inhibition of the dissociation of H_2O_2 to $^{\bullet}OH$ was likely to be the major cause for the lower $^{\bullet}OH$ generation. To confirm this, excess H_2O_2 was added to the suspension in the dark to evaluate the effect of HA on the interaction between H_2O_2 and anatase (Fig. 4c). In

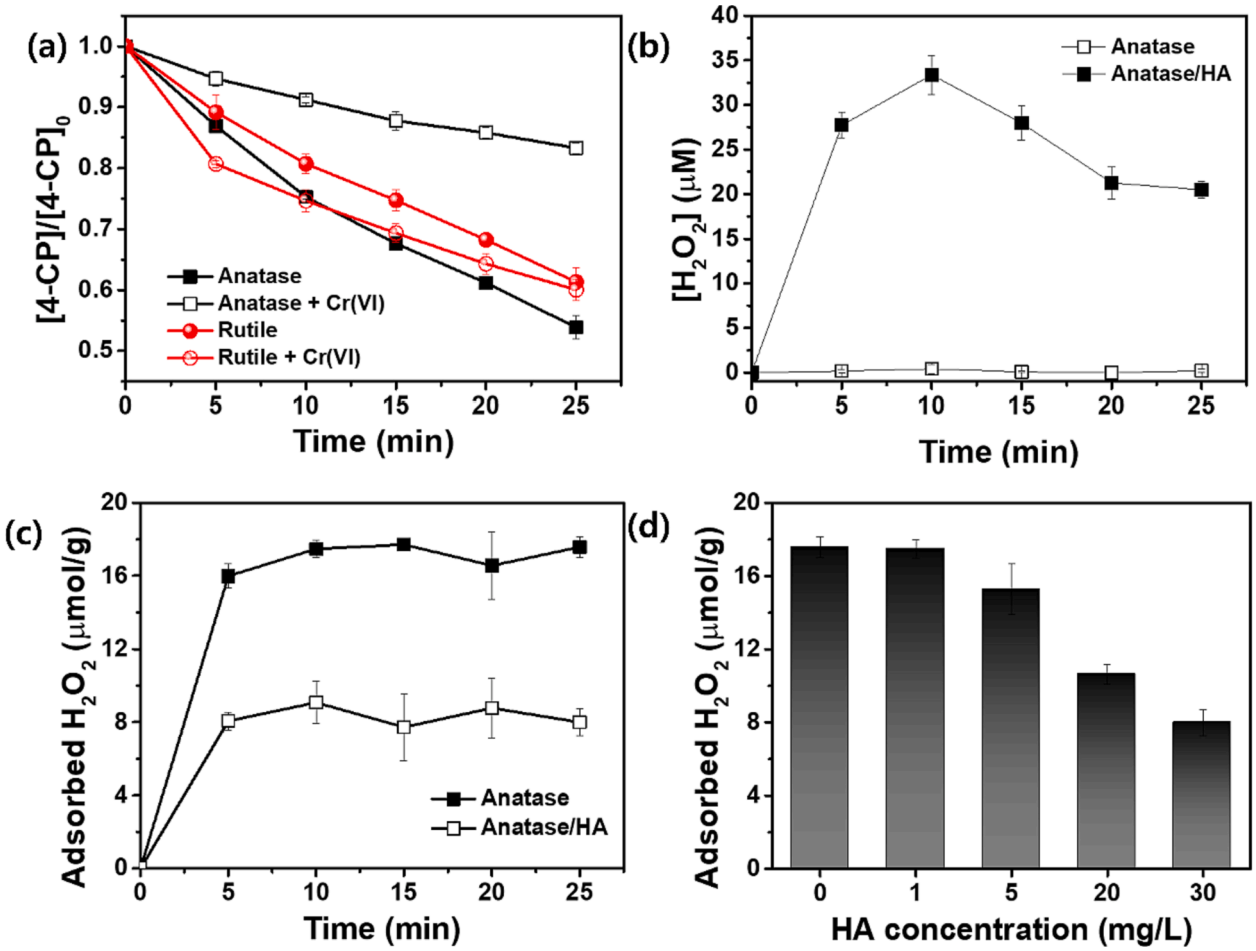

Fig. 4. Different ˙OH generation mechanisms for anatase and rutile are revealed by (a) the addition of Cr(VI) as an electron acceptor (photocatalyst dose = 0.2 g/L), which captures conduction-band electrons that would otherwise initiate ˙OH production via the oxygen reduction (i.e., via superoxide and H_2O_2 formation). (b) The higher accumulation of H_2O_2 (photocatalyst dose = 0.2 g/L, $[HA]_0$ = 20 mg/L), (c) lower H_2O_2 adsorption (photocatalyst dose = 1.0 g/L, $[HA]_0$ = 30 mg/L), and (d) decreased H_2O_2 adsorption with increasing HA concentration indicate that the reaction between H_2O_2 and anatase is the rate-determining step for ˙OH generation (experimental conditions: $[4\text{-CP}]_0$ = 5 mg/L, $[Cr(VI)]_0$ = 1 mM, pH = 6.5 ± 0.2).

the presence of HA, H_2O_2 adsorption onto anatase was hindered due to the blockage of the surface adsorption sites. Additionally, with increasing HA concentration, adsorbed amount of H_2O_2 decreased (Fig. 4d). These results suggest that H_2O_2 generated in situ during UV irradiation is more likely to desorb from the anatase surface, and cannot be reduced further by the conduction band electrons, decreasing ˙OH generation. As a result, due to the enhanced $O_2^{\cdot-}$ generation and lower H_2O_2 dissociation, more H_2O_2 was present in the solution. However, H_2O_2 cannot efficiently oxidize 4-CP due to its relatively low oxidation potential compared to ROS (Fig. S18), consequently decreasing the 4-CP

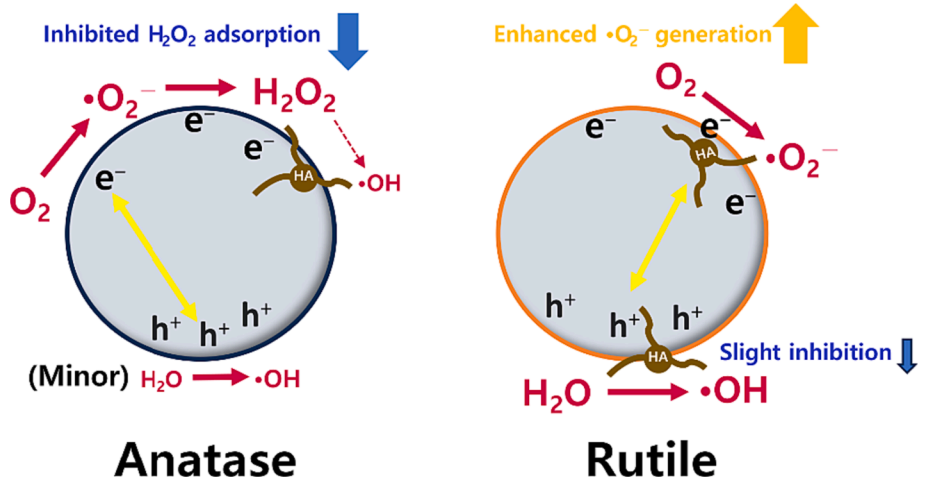

Fig. 5. HA alters ROS generation in a different manner between anatase and rutile.

degradation efficiency of anatase. The addition of HA also increased the H_2O_2 production over rutile, but the H_2O_2 adsorption capacity of rutile was negligible (Fig. S19), which validates that the water oxidation is the major pathway for $^{\bullet}OH$ generation over rutile. The differential effect of HA on ROS generation pathways over anatase versus rutile are illustrated in Fig. 5.

4. Conclusions

Interactions between photocatalysts and NOM are common and influential in photocatalytic water treatment. Here, we show that the crystalline phase of TiO_2 is a critical determinant of susceptibility to performance inhibition by surface-adsorbed HA, by affecting photocatalytic ROS generation pathways. Specifically, we demonstrated that surface-adsorbed HA was the main driver of the observed changes in ROS generation patterns and 4-CP degradation efficiency. Despite similar HA adsorption mechanisms and charge transfer for anatase and rutile, changes to the ROS generation pathways for these two polymorphs led to differences in their overall photocatalytic activity. The O_2 reduction pathway for $^{\bullet}OH$ generation by anatase was inhibited due to the competitive adsorption by H_2O_2 and HA. In contrast, rutile mainly generated $^{\bullet}OH$ via H_2O oxidation, which is less affected by surface-adsorbed HA. Interestingly, photocatalytic 4-CP degradation with rutile was enhanced by HA adsorption (when added at lower concentrations than 20 mg/L) due to of significantly higher $O_2^{\bullet-}$ production.

While anatase is generally considered more advantageous than rutile for the photocatalytic oxidation of organic compounds, the differential effect of NOM on these two TiO_2 phases has been overlooked. We demonstrated that the strong inhibition of anatase by HA resulted in lower photocatalytic activity compared with less-susceptible rutile for the degradation of a target organic pollutant. However, this does not mean that rutile is the best choice for treating real water with NOM, because of its lower intrinsic photocatalytic oxidation activity. Furthermore, HA adsorption may lead to a remarkable increase in H_2O_2 generation of with anatase, which could enhance the effectiveness of hybrid systems (e.g., Fenton/UV/TiO_2) [57] and microbial inactivation [14]. Consequently, further research is needed to explore strategies that mitigate the inhibitory effects of HA to TiO_2 and improve photocatalytic treatment. Meanwhile, this work provides valuable mechanistic insight about the interaction of HA with two different, common crystalline phases of TiO_2, which can inform photocatalytic materials selection and help enable more efficient application of TiO_2 in different water treatment scenarios.

Funding

This work was supported by the National Research Foundation of Korea (NRF-2021R1F1A1063535), and partial support for PA was provided by the NSF ERC on Nanotechnology-Enabled Water Treatment (EEC-1449500).

Declaration of Competing Interest

The authors declare that they have no known competing financial interests or personal relationships that could have appeared to influence the work reported in this paper.

Data availability

Data will be made available on request.

Appendix A. Supplementary data

Supplementary data to this article can be found online at https://doi.org/10.1016/j.cej.2023.146785.

References

[1] B. Li, et al., Photocatalysis driven by near-infrared light: materials design and engineering for environmentally friendly photoreactions, ACS ES&T Eng. 1 (6) (2021) 947–964.
[2] L. Han, et al., Environment friendly and remarkably efficient photocatalytic hydrogen evolution based on metal organic framework derived hexagonal/cubic In_2O_3 phase-junction, Appl. Catal. B 282 (2021), 119602.
[3] D.A. Giannakoudakis, et al., Mechanistic and kinetic studies of benzyl alcohol photocatalytic oxidation by nanostructured titanium (hydro)oxides: Do we know the entire story? Appl. Catal. B 320 (2023), 121939.
[4] Z. Zhang, et al., Modified-pollen confined hybrid system: A promising union for visible-light-driven photocatalytic antibiotic degradation, Appl. Catal. B 330 (2023), 122621.
[5] Q. You, et al., Defects controlling, elements doping, and crystallinity improving triple-strategy modified carbon nitride for efficient photocatalytic diclofenac degradation and H_2O_2 production, Appl. Catal. B 321 (2023), 121941.
[6] C. Zhu, et al., Unveiling spin state-dependent micropollutant removal using single-atom covalent triazine framework, Adv. Funct. Mater. 33 (19) (2023).
[7] Y. Ye, et al., Effect of dissolved natural organic matter on the photocatalytic micropollutant removal performance of TiO_2 nanotube array, J. Photochem. Photobiol. A Chem. 371 (2019) 216–222.
[8] J. Song, et al., The comparative study on inhibitory effect of natural organic matters on the TiO_2 and activated carbon/TiO_2 composites for the removal of 17alpha-ethinylestradiol, Chemosphere 333 (2023), 138930.
[9] K. Yang, D. Lin, B. Xing, Interactions of humic acid with nanosized inorganic oxides, Langmuir 25 (6) (2009) 3571–3576.
[10] X. Yang, et al., Multiple roles of dissolved organic matter in advanced oxidation processes, Environ. Sci. Tech. 56 (16) (2022) 11111–11131.
[11] J. Xu, C.-H. Huang, Enhanced direct photolysis of organic micropollutants by far-UVC light at 222 nm from KrCl* excilamps, Environ. Sci. Technol. Lett. (2023).
[12] Y.-J. Lee, et al., pH-dependent contribution of chlorine monoxide radicals and byproducts formation during UV/chlorine treatment on clothianidin, Chem. Eng. J. 428 (2022), 132444.
[13] X. Wu, et al., Humic acid and fulvic acid hinder long-term weathering of microplastics in lake water, Environ. Sci. Tech. 55 (23) (2021) 15810–15820.
[14] H.T. Bui, et al., Visible-light activation of a dissolved organic matter-TiO_2 complex mediated via ligand-to-metal charge transfer, Environ. Sci. Tech. 56 (15) (2022) 10829–10837.
[15] P. Mazierski, et al., Role of operating parameters in photoelectrocatalytic degradation of anticancer drugs: Ifosfamide, 5-fluorouracil and imatinib using CdS/TiO_2, J. Water Process Eng. 51 (2023), 103460.
[16] S. Xin, et al., Enhanced visible light photoelectrocatalytic degradation of o-chloronitrobenzene through surface plasmonic Au nanoparticles and g-C_3N_4 co-modified TiO_2 nanotube arrays photoanode, Appl. Catal. B 323 (2023), 122174.
[17] L. Rossi, et al., Photocatalytic performance of palladium and carbon modified TiO_2 using solar radiation, J. Photochem. Photobiol. A Chem. 437 (2023), 114461.
[18] Y. Nosaka, A.Y. Nosaka, Generation and detection of reactive oxygen species in photocatalysis, Chem. Rev. 117 (17) (2017) 11302–11336.
[19] Q. Guo, et al., Fundamentals of TiO_2 photocatalysis: concepts, mechanisms, and challenges, Adv. Mater. 31 (50) (2019) e1901997.
[20] M. Rosales, et al., The influence of the morphology of 1D TiO_2 nanostructures on photogeneration of reactive oxygen species and enhanced photocatalytic activity, J. Mol. Liq. 281 (2019) 59–69.
[21] D. Messou, et al., Origin of the synergistic effect between TiO_2 crystalline phases in the Ni/TiO2-catalyzed CO_2 methanation reaction, J. Catal. 398 (2021) 14–28.
[22] Y. Liao, et al., Controllable synthesis of brookite/anatase/rutile TiO_2 nanocomposites and single-crystalline rutile nanorods array, J. Mater. Chem. 22 (16) (2012) 7937.
[23] A. Yamakata, J.J.M. Vequizo, Curious behaviors of photogenerated electrons and holes at the defects on anatase, rutile, and brookite TiO_2 powders: A review, J Photochem Photobiol C: Photochem Rev 40 (2019) 234–243.
[24] I.S. Brandt, et al., Favoring the Reactivity of TiO_2 Films with Ideal Arrangement of Anatase and Rutile Crystallites, ACS Appl. Energy Mater. 2 (4) (2019) 2579–2584.
[25] X. Zhang, et al., Crystal-phase-mediated restructuring of Pt on TiO_2 with tunable reactivity: redispersion versus reshaping, ACS Catal. 12 (6) (2022) 3634–3643.
[26] T. Fu, et al., Zn-CNTs-Cu catalytic in-situ generation of H_2O_2 for efficient catalytic wet peroxide oxidation of high-concentration 4-chlorophenol, J. Hazard. Mater. 401 (2021), 123392.
[27] K. Saravanakumar, et al., Construction of novel In_2S_3/Ti_3C_2 MXene quantum dots/$SmFeO_3$ Z-scheme heterojunctions for efficient photocatalytic removal of sulfamethoxazole and 4-chlorophenol: Degradation pathways and mechanism insights, Chem. Eng. J. 451 (2023), 138933.
[28] B. Ohtani, et al., Isolation of anatase crystallites from anatase-rutile mixed particles by dissolution with aqueous hydrogen peroxide and ammonia, Trans. Mater. Res. Soc. Jpn 32 (2) (2007) 401–404.
[29] T. Ohno, K. Sarukawa, M. Matsumura, Photocatalytic activities of pure rutile particles isolated from TiO_2 powder by dissolving the anatase component in HF solution, J. Phys. Chem. B 105 (12) (2001) 2417–2420.
[30] G.A. Escareno-Torres, et al., Enhanced degradation of ciprofloxacin in water using ternary photocatalysts TiO_2/SnO_2/g-C_3N_4 under UV, visible, and solar light, Environ. Sci. Pollut. Res. (2023).
[31] J.-M. Wu, et al., Synthesizing and comparing the photocatalytic activities of single-crystalline TiO[sub 2] rutile nanowires and mesoporous anatase paste, J. Electrochem. Soc. 154 (3) (2007) H157.

[32] Y.-J. Lee, et al., Simple preparation method for Styrofoam–TiO2 composites and their photocatalytic application for dye oxidation and Cr(VI) reduction in industrial wastewater, Environ. Sci. Water Res. Technol. 7 (1) (2021) 222–230.
[33] Y.J. Lee, et al., Facile synthesis of N vacancy g-C_3N_4 using Mg-induced defect on the amine groups for enhanced photocatalytic $^{\bullet}$OH generation, J. Hazard. Mater. 449 (2023), 131046.
[34] L. Xu, J. Wang, Magnetic nanoscaled Fe_3O_4/CeO_2 composite as an efficient Fenton-like heterogeneous catalyst for degradation of 4-chlorophenol, Environ. Sci. Tech. 46 (18) (2012) 10145–10153.
[35] J. Zhang, et al., New understanding of the difference of photocatalytic activity among anatase, rutile and brookite TiO_2, PCCP 16 (38) (2014) 20382–20386.
[36] G.Z.S. Ling, S.F. Ng, W.J. Ong, Tailor-engineered 2D cocatalysts: harnessing electron-hole redox center of 2D g-C3N4 photocatalysts toward solar-to-chemical conversion and environmental purification, Adv. Funct. Mater. (2022) 2111875.
[37] A. Gautam, et al., Photodegradation of organic dyes based on anatase and rutile TiO_2 nanoparticles, RSC Adv. 6 (4) (2016) 2746–2759.
[38] B. Ohtani, et al., What is degussa (Evonik) P25? Crystalline composition analysis, reconstruction from isolated pure particles and photocatalytic activity test, J. Photochem. Photobiol. A Chem. 216 (2–3) (2010) 179–182.
[39] M. Long, et al., Phosphate changes effect of humic acids on TiO_2 photocatalysis: from inhibition to mitigation of electron-hole recombination, Environ. Sci. Tech. 51 (1) (2017) 514–521.
[40] J. Wiszniowski, et al., Photocatalytic decomposition of humic acids on TiO_2 Part I: Discussion of adsorption and mechanism, J. Photochem. Photobiol. A Chem. 152 (2002) 267–273.
[41] D.D. Sun, P.F. Lee, TiO_2 microsphere for the removal of humic acid from water: Complex surface adsorption mechanisms, Sep. Purif. Technol. 91 (2012) 30–37.
[42] G. Huang, et al., Hydrogen production from natural organic matter via cascading oxic-anoxic photocatalytic processes: An energy recovering water purification technology, Water Res. 175 (2020), 115684.
[43] C. Kim, et al., Activation of persulfate by humic substances: Stoichiometry and changes in the optical properties of the humic substances, Water Res. 212 (2022), 118107.
[44] J.Y. Hwang, et al., Crystal phase-dependent generation of mobile OH radicals on TiO_2: Revisiting the photocatalytic oxidation mechanism of anatase and rutile, Appl. Catal. B 286 (2021), 119905.
[45] S. Lan, et al., Performance and mechanism of piezo-catalytic degradation of 4-chlorophenol: finding of effective piezo-dechlorination, Environ. Sci. Tech. 51 (11) (2017) 6560–6569.
[46] B.M. Lee, Y.S. Seo, J. Hur, Investigation of adsorptive fractionation of humic acid on graphene oxide using fluorescence EEM-PARAFAC, Water Res. 73 (2015) 242–251.
[47] X. Yang, et al., Fouling of TiO_2 induced by natural organic matters during photocatalytic water treatment: Mechanisms and regeneration strategy, Appl Catal B 294 (2021), 120252.
[48] T. Liu, et al., Water decontamination via nonradical process by nanoconfined Fenton-like catalysts, Nat. Commun. 14 (1) (2023) 2881.
[49] Y.-J. Lee, et al., Enhancement of photocatalytic Cr(VI) reduction using mandarin peel extract as natural sacrificing agent, Alex. Eng. J. 75 (2023) 151–163.
[50] T. Hirakawa, K. Yawata, Y. Nosaka, Photocatalytic reactivity for O^{2-} and OH radical formation in anatase and rutile TiO_2 suspension as the effect of H_2O_2 addition, Appl. Catal. A 325 (1) (2007) 105–111.
[51] M. Buchalska, et al., On Oxygen Activation at Rutile- and Anatase-TiO_2, ACS Catal. 5 (12) (2015) 7424–7431.
[52] C. Tao, et al., Tunable selectivity of radical generation over TiO_2 for photocatalysis, Chem. Eng. Sci. 214 (2020), 115438.
[53] W.F. Huang, P. Raghunath, M.C. Lin, Computational study on the reactions of H2O2 on TiO2 anatase (101) and rutile (110) surfaces, J. Comput. Chem. 32 (6) (2011) 1065–1081.
[54] W. Kim, et al., Molecular-level understanding of the photocatalytic activity difference between anatase and rutile nanoparticles, Angew. Chem. Int. Ed. 53 (51) (2014) 14036–14041.
[55] Y.-J. Lee, et al., Photocatalytic degradation of neonicotinoid insecticides using sulfate-doped Ag_3PO_4 with enhanced visible light activity, Chem. Eng. J. 402 (2020), 126183.
[56] Y. Hu, et al., What Controls Direct Hole-Mediated Oxidation Kinetics in a Carbon Nitride-Based Photocatalytic System: A Model Study for Aqueous Aromatic Compounds, ACS Catal. 13 (18) (2023) 12269–12280.
[57] B. Zhao, et al., Degradation of trichloroacetic acid by an efficient Fenton/UV/TiO_2 hybrid process and investigation of synergetic effect, Chem. Eng. J. 273 (2015) 527–533.